Multiscale Mechanical Characterization of 3D-Printed Composite for Calibration and Validation of a Phase-Field Model

E. Kerino[1], D. Therriault[1] and M. Lévesque[1*]

[1] Laboratory for Multiscale Mechanics (LM2), Mechanical Engineering Department,

Polytechnique Montreal, 2900 boul. Edouard-Montpetit, Montreal, QC, Canada

* *Corresponding author (martin.levesque@polymtl.ca)*

Keywords: *Fused filament fabrication; Mechanical characterization; Digital image correlation; Short fiber-reinforced composites; Fracture mechanics*

1. Abstract

Fused Filament Fabrication (FFF) enables the production of lightweight composite components for some aerospace applications. However, the layer-by-layer deposition process introduces microstructural heterogeneities that complicate the prediction of fracture behavior. Phase-field fracture models constitute a promising numerical framework for simulating crack propagation in FFF-fabricated parts, but their calibration and validation require reliable experimental data at multiple scales. This study presents a two-scale mechanical characterization of short carbon fiber-reinforced Polyetherimide (PEI-CF) specimens fabricated by FFF at multiple build orientations. At the macroscale, tensile tests following ASTM D638 were used to determine the Young's modulus at three printing orientations, and Compact Tension (CT) tests following ASTM D5045 were used to measure the mode-I critical energy release rate G_{Ic} at two printing angles ($\alpha = 0°$ and $\alpha = 90°$). At the mesoscale, full-field displacement and strain measurements were obtained by stereoscopic Digital Image Correlation (DIC) during CT specimen fracture, complemented by optical micrographs of the fracture surfaces. The macroscale results revealed a strong process-induced anisotropy. The Young's moduli ranged from 5210 MPa in the bulk orientation to 2689 MPa in the inter orientation. The G_{Ic} values showed an approximately 2.1-fold increase from $\alpha = 0°$ (1.76 ± 0.31 kJ/m²) to $\alpha = 90°$ (3.65 ± 0.37 kJ/m²), attributed to a more energy-intensive fracture mechanism at 90° (fiber pull-out), as the crack propagated across the printed layers. The DIC measurements confirmed the mode I fracture pattern at both orientations. The fracture surface micrographs revealed crack propagation along the interlayer interface at $\alpha = 0°$, with both micro- and macro-porosities visible, and a zig-zag crack path at $\alpha = 90°$, driven by competing failure mechanisms between intra-layer macro-porosities and weak interlayer bonds. The resulting two-scale dataset provides both calibration inputs and quantitative validation references for phase-field fracture models of FFF-printed PEI-CF composites.

2. Introduction

Fused Filament Fabrication (FFF) is an additive manufacturing process that produces complex, lightweight, and functional polymeric and composite components [1], [2]. Its geometric versatility and relatively low manufacturing cost make FFF an increasingly attractive process for some applications in the aerospace and industrial sectors. Among the most promising candidate materials are Polyetherimide (PEI) and its carbon fiber-reinforced counterpart (PEI-CF), which combine high mechanical performance with thermal stability (operating temperature up to 170 °C).

The layer-by-layer deposition strategy inherent to the FFF process introduces significant microstructural heterogeneities, including mechanical anisotropy, intra-layer porosities, and interlayer adhesion defects [3]. These features substantially complicate the prediction of fracture behavior in additively manufactured structures. Robust numerical frameworks, such as phase-field fracture models [4], constitute promising approaches for simulating crack propagation in FFF-fabricated components. Their predictive accuracy depends on the reliability of the experimental data, both as model inputs and as validation references.

This work proposes a macro- and mesoscale mechanical characterization of the elastic and fracture properties. At the macroscale, key mechanical properties are measured, namely the Young's modulus E and the mode-I critical energy release rate G_{Ic}. At the mesoscale, full-field characterization is performed, including displacement and strain field measurements while pre-cracked specimens are mechanically loaded.

Standardized test protocols provide the experimental framework for macroscale property measurement. The ASTM D638 standard [5] prescribes a type I dogbone specimen geometry and testing conditions for the determination of the Young's modulus. The critical energy release rate G_{Ic} is determined in accordance with the ASTM D5045 standard [6], which specifies specimen geometries such as the Compact Tension (CT) configuration. In both cases, the directional dependence of the mechanical response caused by FFF-induced anisotropy necessitates testing at a minimum of two distinct printing orientations to ensure comprehensive characterization.

At the mesoscale, Digital Image Correlation (DIC) is utilized to obtain full-field surface displacement and strain measurements during mechanical testing of CT specimens. The resulting spatially resolved experimental fields serve as direct quantitative benchmarks against predictions derived from numerical models developed by our team, thereby providing a rigorous basis for model validation [7], [8].

This study therefore provides a macro- and mesoscale experimental dataset for FFF-printed PEI-CF, suitable for calibrating and validating phase-field fracture models.

3. Methodology

3.1. Material and specimen manufacturing

The material used in this study is Polyetherimide (PEI), commercially known as Ultem 1010, reinforced with short carbon fibers. It was supplied as 1.75 mm diameter filaments (PEI-CF, Nanovia, France) in 500 g spools and dried at 80 °C for at least 48 h prior to printing. The fiber volume fraction of the filament was measured by micro-tomography and was equal to ~11.8 vol.%. The fibers had an average length of approximately 24 µm. Specimens were fabricated on an AON3D Hylo printer (Canada) and sliced with PrusaSlicer. The printing parameters, summarized in Table 1, were selected to maximize inter-layer and intra-layer adhesion. The specimens were printed infill only, without perimeters or solid top and bottom layers found on default 3D-printed parts. These elements served, in most cases, an aesthetic purpose only and thus were omitted from our prints.

Two types of specimens were prepared. The first were type I dogbone specimens, fabricated in accordance with the ASTM D638 standard [5]. Figure 1a shows the three build orientations investigated: the bulk orientation, where filaments are deposited along the loading axis; the interface (or inter) orientation, where filaments are deposited perpendicular to it; and the 45° orientation, which represents an intermediate case. Figure 1b provides the specimen dimensions together with a schematic of the filament extrusion direction.

Table 1. Printing parameters used for the fabrication of PEI-CF dogbones and CT specimens on the AON3D Hylo printer.

Temperatures [°C]			Extrusion multiplier	Nozzle diameter [mm]	Layer height [mm]	Printing speed [mm/s]	Infill
Nozzle	Bed	Chamber					
390	210	210	1.15	0.6	0.3	50	100% rectilinear with 0° raster angle

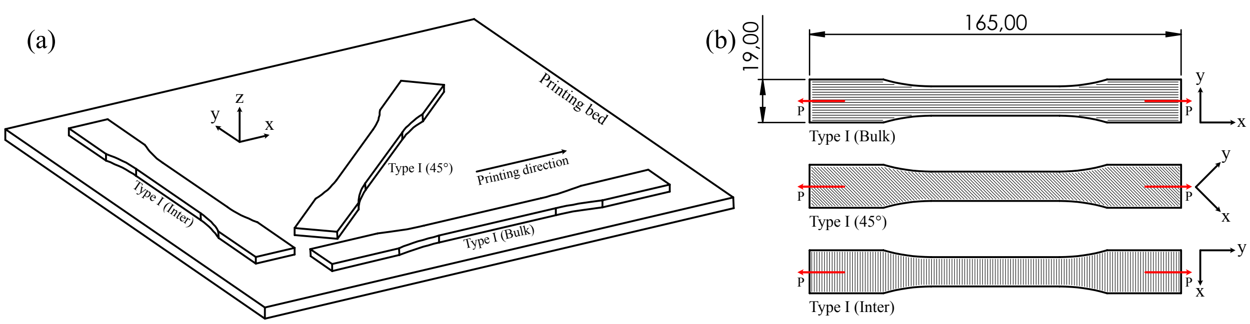

Figure 1. (a) Build orientations of the type I dogbone specimens; (b) specimen dimensions and filament deposition direction, the thickness is 3.2 mm for all the printed dogbones.

The second specimen type was the compact tension (CT) specimen, fabricated in accordance with the ASTM D5045 standard [6]. Figure 2a shows the two build orientations investigated, where α denotes the angle between the pre-crack direction and the printed layers (as shown in Figure 2c). Prior to testing, a sharp pre-crack was introduced at the notch tip by the razor tapping method, as described in [6]. Figure 2b provides the specimen dimensions.

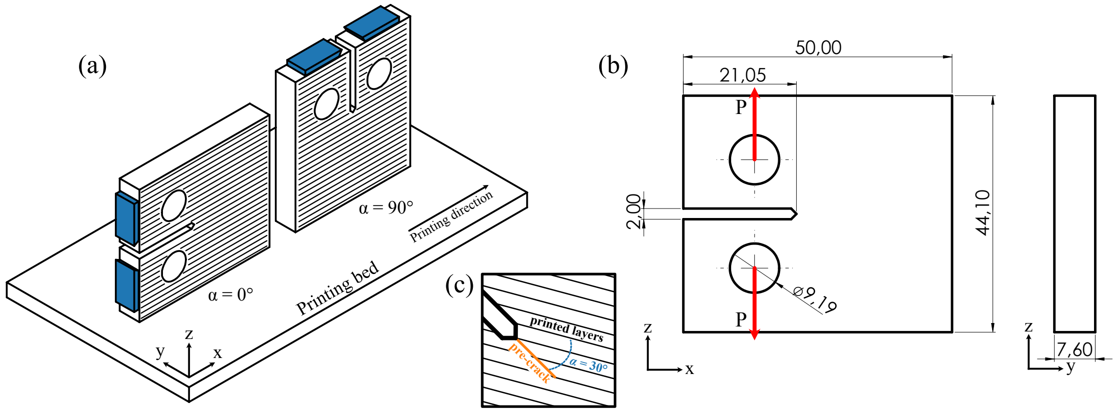

Figure 2. (a) Build orientations of the CT specimens investigated, 3D-printed knife edges glued post-printing to the notched face are indicated in blue; (b) CT specimen dimensions; (c) schematic description of the printing angle α.

3.2. Macroscale mechanical testing

Tensile tests were conducted following the ASTM D638 standard. Prior to testing, the cross-sectional dimensions of each specimen were measured with a digital caliper (Mitutoyo 500-196-30, Japan). Tests were performed on an MTS Insight electromechanical machine fitted with a 50 kN load cell and an MTS 634.25F-25 extensometer. A displacement rate of 5 mm/min was applied, and an initial pre-load of approximately 100 N was used to eliminate mechanical gaps between the specimen and the fixture pins.

CT tests were conducted following the ASTM D5045 standard. Specimen dimensions were measured prior to testing; however, the notch and pre-crack lengths were determined post-failure from optical microscope images, following the procedure described in ASTM E399 [9]. Tests were performed on the same testing machine, equipped with an MTS 632.02E-20 Crack Opening Displacement (COD) extensometer. The knife edges shown in Figure 2 were used to seat the two extensometer arms in their initial position. A displacement rate of 10 mm/min was applied, and an initial pre-load of approximately 40 N was used to eliminate mechanical gaps between the specimen and the fixture pins.

3.3. Mesoscale mechanical testing with digital image correlation

Stereoscopic DIC tests were performed on CT specimens prepared following the methodology described above. After pre-cracking, CT specimens were polished on a Buehler Metaserv 2000 with three grit sizes of CarbiMet abrasive paper: P60, P120 and P280. Then, two coats of Rust-Oleum flat white paint were sprayed, and a black speckle pattern was added using a Timbertech ABPST01 airbrush. The black paint used was Golden Carbon Black paint, at a 2:1 dilution ratio.

The CT specimens were then tested on a DIC setup, consisting of two Basler Ace acA2440-75um cameras equipped with Fujinon HF75SA-1 lenses and 20 mm extension tubes. The images were captured at 1 fps using Vic-Snap (Correlated Solutions) software. The test rate was set to 0.05 mm/min under closed-loop control using the COD extensometer. Due to its brittle nature, PEI-CF was tested at this low rate to ensure stable crack propagation, allowing multiple images to be captured during crack propagation. The ROI extracted from Vic-3D 9 (Correlated Solutions) was 30×10 mm^2. A subset size of 37 to 41 pixels, a step size of 7 pixels and a strain filter of 15 pixels were used. The vertical displacement V and the vertical Lagrangian strain ε_{yy} were then extracted.

Optical micrographs were then acquired using a Keyence VHX-7000 microscope at 100× magnification to characterize the crack path morphology, with both side and top views of each cracked specimen.

4. Results and Discussion

4.1. Macroscale mechanical testing

Figure 3 presents the results of the mechanical characterization. For the CT tests (Figure 3a), the load-displacement curves confirm the brittle fracture behavior of PEI-CF for both build orientations. The maximum loads recorded for the 90° specimens were higher than those for the 0° specimens, consistent with the higher critical energy release rate measured at this orientation. For the tensile tests (Figure 3b), the bulk orientation specimens exhibited the highest stiffness and a brittle fracture response, while the inter orientation specimens showed the lowest Young's modulus, consistent with loading applied perpendicular to the filament deposition direction. The stress-strain curves also displayed less scatter than the CT load-displacement results. The mechanical properties extracted from both test types are summarized in Table 2.

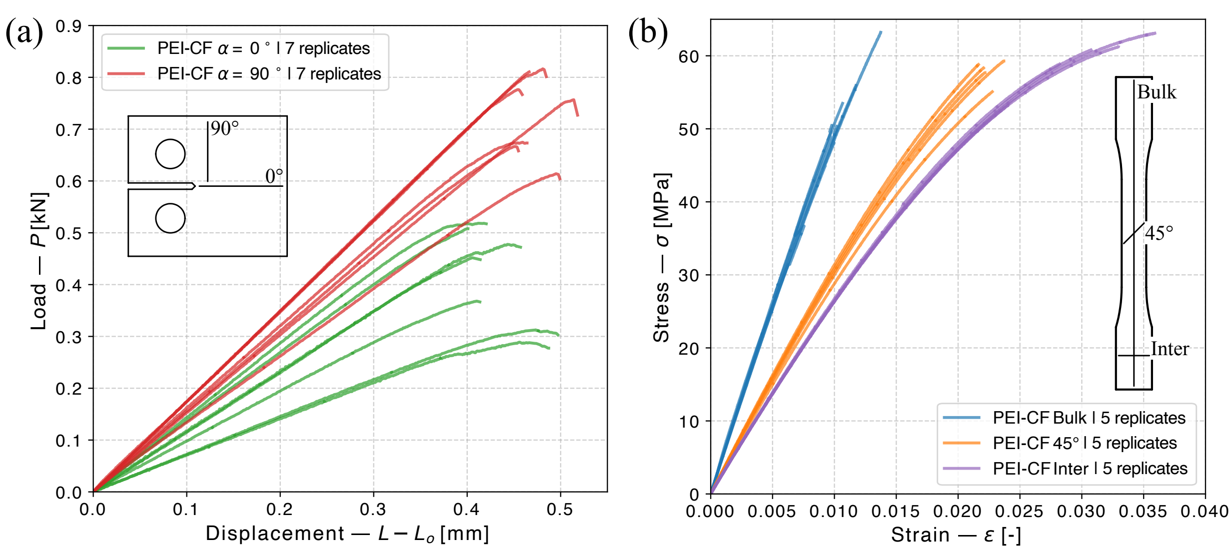

Figure 3. (a) Load-displacement curves from the CT fracture tests for both build orientations; (b) Stress-strain curves from the tensile tests for the three build orientations.

Table 2 reports the macroscale mechanical properties of FFF-printed PEI-CF. The G_{Ic} values reveal a strong process-induced anisotropy: $G_{Ic}^{90°}$ (3.65 kJ/m²) is approximately 2.1 times higher than $G_{Ic}^{0°}$ (1.76 kJ/m²). The difference reflects the activation of a more energy-intensive fracture mechanism at 90°, whereas at 0° the crack follows the weaker interlayer bonding plane. The 2.1 ratio is consistent with values reported in the literature for short fiber-reinforced composites produced by FFF [7], [8], and constitutes a critical input parameter for calibrating phase-field fracture models. Regarding the tensile properties, the Young's modulus decreases from the bulk orientation (5210 MPa) to the inter orientation (2689 MPa), a reduction of approximately 48 %.

Table 2. Critical energy release rate and elastic properties of FFF-printed PEI-CF. The G_{Ic} values represent the average of 7 replicates, and the Young's modulus values represent the average of 5 replicates. Both properties include 95% confidence intervals.

$G_{Ic}^{0°}$ (kJ/m²)	$G_{Ic}^{90°}$ (kJ/m²)	E_{Bulk} (MPa)	$E_{45°}$ (MPa)	E_{Inter} (MPa)
1.76 [±0.31]	3.65 [±0.37]	5210 [±126]	3149 [±116]	2689 [±76]

4.2. Full-field mesoscale mechanical testing

Figure 4 presents the DIC results for a CT specimen fabricated at $\alpha = 0°$ undergoing mode I loading at three different time steps. The two fields presented are the Lagrangian vertical strain ε_{yy} and the vertical displacement V. In the strain field shown in Figure 4b and c, the characteristic lobe distribution associated with mode I fracture is observed, as well as stress concentration at the crack tip. The optical micrographs in the bottom row of Figure 4 provide further detail on the fracture

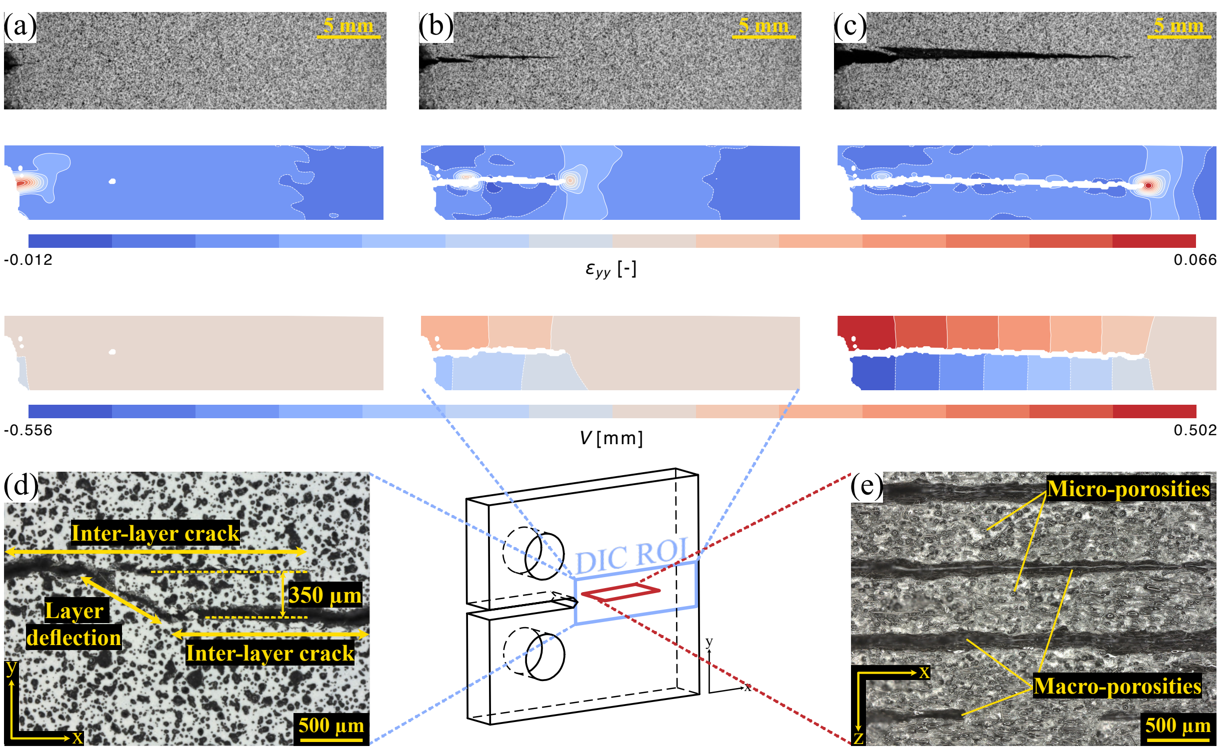

Figure 4. Full-field strain (ε_{yy}) and vertical displacement (V) maps obtained from DIC measurements on CT specimens with α = 0°, showing interlayer crack propagation at three successive time steps: (a), (b), and (c). The bottom row provides a schematic of the region of interest (ROI) on the CT specimen, along with two optical micrographs (100x magnification): (d) a side view of the crack path and (e) a top view of the fracture surface.

morphology. On the side view of Figure 4d, the crack exhibits a slight deviation, jumping onto the layer below, but generally propagates along the interlayer interface. On the top view of Figure 4e, both micro-porosities (defects originating from the filament material prior to printing) and macro-porosities (intra-layer voids between adjacent extruded paths) are visible on the fractured surface.

Figure 5 presents the DIC results for a CT specimen fabricated at α = 90°, in which crack propagation occurred across the printed layers. The characteristic lobe distribution and the stress concentration at the crack tip are also observed in Figure 5b and c. The optical micrographs in Figure 5 reveal additional features of the fracture surface. On the side view of Figure 5d, numerous short carbon fibers are observed extending from the crack faces, consistent with a fiber pull-out mechanism. The fiber pull-out is one of the energy-intensive mechanisms responsible for the increase in G_{Ic} between the two orientations. The crack also follows a zig-zag path rather than propagating in a straight line. On the top views of Figure 5e and f, numerous macro-porosities are present, including one notably large pore (Figure 5e) likely resulting from the coalescence of multiple stacked intra-layer macro-porosities, which created stress concentration sites for crack propagation.

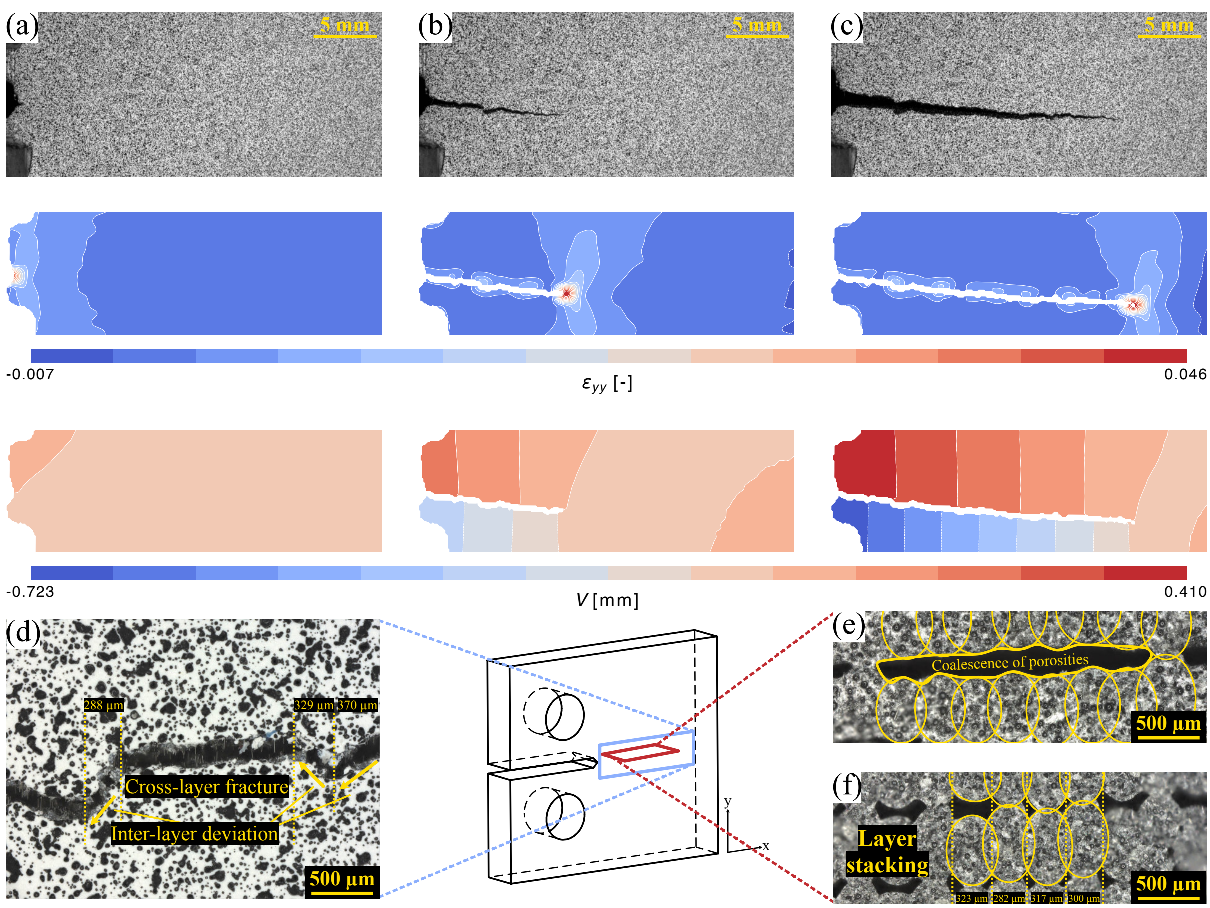

Figure 5. Full-field strain (ε_{yy}) and vertical displacement (V) maps obtained from DIC measurements on CT specimens with α = 90°, showing crack propagation across the printed layers at three successive time steps: (a), (b), and (c). Optical micrographs (100x magnification) in the bottom row provide complementary views of the fracture: (d) a side view of the crack path, and (e, f) top views of the fracture surface.

When compared to the $\alpha = 0°$ configuration, in which the crack propagated predominantly along the interlayer interface, the crack path in the $\alpha = 90°$ specimens deviated from a straight direction, alternating between cross-layer failure and interlayer deviation. The zig-zag propagation pattern has been reported in the literature for FFF-fabricated short fiber-reinforced composites [7]. The zig-zag behavior can be attributed to competing failure mechanisms: intra-layer macro-porosities deflect the crack across the layers, while weak interlayer bonds redirect it toward the interface. It should also be noted that the DIC measurements were performed at a displacement rate of 0.05 mm/min, significantly lower than the 10 mm/min rate specified in [6] and applied in the macroscale CT tests. The lower rate was deliberately chosen to ensure stable crack propagation and enable image capture throughout the test. At this rate, PEI-CF exhibited a more ductile response involving limited plastic deformation, which should be considered when using these full-field measurements as quantitative validation references for computational models.

5. Conclusion

This study presented a two-scale mechanical characterization of FFF-printed PEI-CF at two build orientations, providing an experimental dataset for the calibration and validation of phase-field fracture models.

At the macroscale, tensile and CT fracture tests revealed a strong process-induced anisotropy. The Young's modulus ranged from 5210 MPa in the bulk orientation to 2689 MPa in the inter orientation, a reduction of approximately 48 %. The critical energy release rate G_{Ic} increased by a factor of approximately 2.1 from $\alpha = 0°$ (1.76 kJ/m²) to $\alpha = 90°$ (3.65 kJ/m²), reflecting the activation of a more energy-intensive fracture mechanism when the crack propagated across the printed layers.

At the mesoscale, stereoscopic DIC confirmed a mode I fracture pattern at both orientations. The fracture surface micrographs revealed distinct failure modes depending on build orientation: at $\alpha = 0°$, the crack propagated along the interlayer interface, with micro- and macro-porosities visible on the fracture surface; at $\alpha = 90°$, a zig-zag crack path was observed, driven by competing failure mechanisms between intra-layer macro-porosities and weak interlayer bonds, accompanied by fiber pull-out. These mesoscale observations are consistent with the higher G_{Ic} value measured at $\alpha = 90°$.

Collectively, the macroscale elastic and fracture properties alongside the mesoscale full-field measurements provide a multiscale experimental dataset specifically suited to the calibration and validation of phase-field fracture models for FFF-printed PEI-CF composites. This contribution is especially significant considering the growing recognition of phase-field models as one of the most promising approaches to crack propagation simulation in additively manufactured composites.

The main experimental challenge encountered in this study was ensuring sufficiently stable crack propagation to enable the acquisition of multiple images during crack growth, given the use of conventional, non-high-speed cameras in the DIC setup. Future work could address this limitation by coupling high-speed imaging with the DIC system, which would extend the applicability of the full-field measurements to faster, more unstable fracture events representative of in-service loading conditions.

6. Acknowledgements

We acknowledge the assistance of Dr. Dogan Arslan and Minh-Tam Nguyen for the selection of the PEI-CF printing parameters and the micro-tomography data. We acknowledge the financial and technical support of Safran Group and Dyze Design, and the financial support of NSERC (ALLRP 581752 - 23) and Prima Québec (R25-13-003-PME).

7. References

[1] B. Brenken, E. Barocio, A. Favaloro, V. Kunc, and R. B. Pipes, "Fused filament fabrication of fiber-reinforced polymers: A review," *Addit. Manuf.*, vol. 21, pp. 1–16, May 2018, doi: 10.1016/j.addma.2018.01.002.

[2] L. G. Blok, M. L. Longana, H. Yu, and B. K. S. Woods, "An investigation into 3D printing of fibre reinforced thermoplastic composites," *Addit. Manuf.*, vol. 22, pp. 176–186, Aug. 2018, doi: 10.1016/j.addma.2018.04.039.

[3] R. J. Zaldivar, D. B. Witkin, T. McLouth, D. N. Patel, K. Schmitt, and J. P. Nokes, "Influence of processing and orientation print effects on the mechanical and thermal behavior of 3D-Printed ULTEM® 9085 Material," *Addit. Manuf.*, vol. 13, pp. 71–80, Jan. 2017, doi: 10.1016/j.addma.2016.11.007.

[4] O. Lampron, D. Therriault, and M. Lévesque, "Phase-field modeling of fracture in fused filament fabricated thermoplastic parts and experimental validation," *Eng. Fract. Mech.*, vol. 292, p. 109667, Nov. 2023, doi: 10.1016/j.engfracmech.2023.109667.

[5] ASTM Standards, *Test Method for Tensile Properties of Plastics*, D638. doi: 10.1520/D0638-14.

[6] ASTM Standards, *Test Methods for Plane-Strain Fracture Toughness and Strain Energy Release Rate of Plastic Materials*, D5045. doi: 10.1520/D5045-14R22.

[7] A. Lingua, F. Sosa-Rey, S. Pautard, D. Therriault, and M. Lévesque, "Multiscale characterization of the fracture mechanics of additively manufactured short fiber-reinforced composites," *Eng. Fract. Mech.*, vol. 289, p. 109343, Sep. 2023, doi: 10.1016/j.engfracmech.2023.109343.

[8] O. Lampron, A. Lingua, D. Therriault, and M. Lévesque, "Characterization of the non-isotropic tensile and fracture behavior of unidirectional polylactic acid parts manufactured by material extrusion," *Addit. Manuf.*, vol. 61, p. 103369, Jan. 2023, doi: 10.1016/j.addma.2022.103369.

[9] ASTM Standards, *Standard Test Method for Linear-Elastic Plane-Strain Fracture Toughness of Metallic Materials*, E399. doi: 10.1520/E0399-24.